Applied Mathematical Modelling 40 (2016) 4505–4523

Contents lists available at ScienceDirect

Applied Mathematical Modelling

journal homepage: www.elsevier.com/locate/apm

Nonlinear coupled dynamics of an asymmetric double-disc rotor-bearing system under rub-impact and oil-film forces

Ling Xiang [a,*], Aijun Hu [a], Lanlan Hou [a], Yeping Xiong [b], Jingtang Xing [b]

[a] Department of Mechanical Engineering, North China Electric Power University, Baoding 071003, Hebei Province, China
[b] Faulty of Engineering and the Environment, University of Southampton, Southampton SO16 7QF, UK

ARTICLE INFO

Article history:
Received 1 September 2014
Revised 30 June 2015
Accepted 9 November 2015
Available online 2 December 2015

Keywords:
Rotor-bearing system
Nonlinear dynamics
Bifurcation
Rub-impact
Oil-film forces

ABSTRACT

The nonlinear dynamic behavior of an asymmetric double-disc rotor-bearing system with interaction between rub-impact and oil-film forces is addressed in this paper. Using dynamics theory, the mathematical model of an asymmetric double-disc rotor-bearing system is established, considering nonlinear oil-film force and rub-impact force. The nonlinear oil-film force model is presented in Reynolds equation, and the rub-impact is assumed with a Hertz contact and a Coulomb friction. The dynamic equations with coupled rub-impact and oil-film forces are numerically solved using the Runge–Kutta method. Bifurcation diagrams, largest Lyapunov exponent, Poincaré maps, and three-dimension spectral plots are employed to analyze the dynamic behavior of the system. The sub-harmonic, multiple periodic, quasi-periodic and chaotic motions are observed in this study. A special phenomenon is occurring that the motion of system becomes simple and the oil-whirl is restrained or even removed with an increasing imbalance by magnifying the eccentricity. Another special phenomenon is also occurring that the oil-whirl gets diminished or even disappeared with increasing stator stiffness, but the oil-whip is uninfluenced. The discoveries will have a considerable value as diagnostic tools in settling oil-film instability. The numerical results show that the nonlinear dynamic behavior of the system varies with the rotational speed and model parameters.

1. Introduction

Rotating machineries are the key equipments that are used in diverse engineering fields. The stability of bearing-rotor system is a very important issue for design, manufacturing, and operation of rotating machinery. The instability of bearing-rotor system will result in strong vibration and even disastrous accident of machinery. For decades the researches indicate that the nonlinear exciting sources such as oil-film forces, sealing forces and nonuniform steam forces et al. are main reasons which can make unstable accidents in rotating machineries. The oil-film forces are the leading nonlinear exciting source which makes the bearing-rotor system to be a self-exciting vibration system and results in fatal accidents. The rub-impact is one of the common nonlinear faults in rotor systems, and can bring a serious hazard to machines. Under many circumstances, the rub-impact usually results from excessive vibration caused by other faults in practical rotor systems, such as imbalance, rotor crack, and oil-film instability. The rotor-bearing model takes the nonlinear oil-force into account but the other fault such as rub impact force may be neglected. In modern industry, the machinery is becoming more and more precise with the increasing development of science

* Corresponding author. Tel.: +86 15032496266; fax: +86 03127525016.
E-mail address: ncepuxl@163.com (L. Xiang).

http://dx.doi.org/10.1016/j.apm.2015.11.028
S0307-904X(15)00742-8/

Nomenclature

σ	Somerfield revision number
R	radius of bearing (m)
c	bearing radial clearance (m)
f	friction coefficient
μ	lubricating oil viscosity (Pa · s)
$\delta.$	clearance between rotor and stator
K_c	stator stiffness
L	length of bearing (m)
D	bearing diameter (m)
E	Young's modulus (Pa)
l_1	length of the first axis (m)
l_2	length of the second axis (m)
l_3	length of the third axis (m)
m_1 m_4	mass of bearings (kg)
m_2 m_3	mass of discs (kg)
$[M]$	mass matrix of the system
$[C]$	damping matrix of the system
$[K]$	stiffness matrix of the system
c_i	damping coefficient ($N \cdot s \cdot m^{-1}$)
I_i	section inertia of axis (m^4)
$[F_o]$	plural oil-film force matrix
$[F_p]$	plural rub-impact force matrix
$[F_g]$	plural gravity matrix
b_2 b_2	the mass eccentricity of discs (mm)

and technology. The faults of these machineries are also becoming complicated, and the multiple or coupled faults often occur at the same time. So the dynamic behaviors of the bearing-rotor should be studied considering rub-impact and oil-film forces.

There are a lot of researches in analyzing the nonlinear dynamic of rotor-bearing system. Ehrich [1] studied about the bifurcation of a bearing-rotor system identifying a subharmonic vibration phenomenon in a rotor dynamic system. Diken [2] presented the non-linear vibration analysis and subharmonic whirl frequencies of the Jeffcott rotor mode. Wang et al. [3] analyzed the nonlinear dynamic of a flexible rotor supported by externally pressurized porous gas journal bearings. They demonstrated periodic and quasi-periodic response of journal and rotor center. Whirl and whip instabilities were studied in rotor-bearing system considering a nonlinear force model [4]. The motion equations have been established for symmetrical single-disk flexible rotor-bearing system, and nonlinear oil-film forces of finite journal bearings are calculated [5]. The motion stability of the flexible rotor-bearing system was analyzed with two unbalanced disks [6]. Experiment was observed on fault detection for a direct coupled rotor-bearing system [7]. The non-linear dynamic behaviors of a rotor-bearing coupled system were reported in simulation and experiment [8]. Study of start-up vibration response for oil whirl, oil whip and dry whip was presented in [9]. These researches demonstrated that it is important to study the nonlinear dynamic of rotor-bearing, but the continue work is necessary to be developed, in which the analysis should be made taking into account the dynamic behavior of a rotating system under the oil whirl and oil whip phenomenon, considering the influence of unbalance, model parameters and other fault forces.

The dynamics of rotor to stator contact-dynamics have been studied extensively in the past by many researches. Muszynska [10] presented a comprehensive literary survey on rub-related phenomena. In the 90s a great deal of work treated the nonlinear analysis on rotor to stator contact dynamics. Studies on these rubbing phenomena revealed that the rotating system showed a rich class of nonlinear related dynamics such as sub and super-synchronous responses, quasi-periodic responses and even chaotic motions. Goldman and Muszynska [11] reported that the chaotic motion in a nonlinear study is more likely to occur if a proper impact model is employed. Chu and Zhang [12] investigated the nonlinear vibration characteristics of a rub-impact Jeffcott rotor. They also found that when the rotating speed is increased, the grazing bifurcation, the quasi-periodic motion and chaotic motion occur after the rub-impact. Issam [13] used numerical analysis and evolutionary algorithms to analyze the nonlinear dynamics of a rotor with rub-impact. Chaos and bifurcation of a flexible rub-impact rotor were reported, and the rotor was supported by oil film bearings with nonlinear suspension [14]. Lahriri [15-16] conducted the experimental quantification of contact forces and theoretical analysis of rub-impact rotor-bearing system. The study [17] performed a dynamic analysis of the rub-impact rotor supported by two couple stress fluid film journal bearings, and the strong nonlinear couple stress fluid film force, nonlinear rub-impact force and nonlinear suspension (hard spring) are presented and coupled together.

Of the existing work, some researches [17-19] have thrown light to nonlinear coupled or interaction dynamics considering different forces or different influences, but little research has been carried out on nonlinear coupled dynamics of an asymmetric double-disc rotor-bearing system considering rub-impact and oil-film forces. The studies on interaction of rub-impact and oil-film instability are still not enough either in numerical analysis or in experimental results. Thus, some new attempt will be

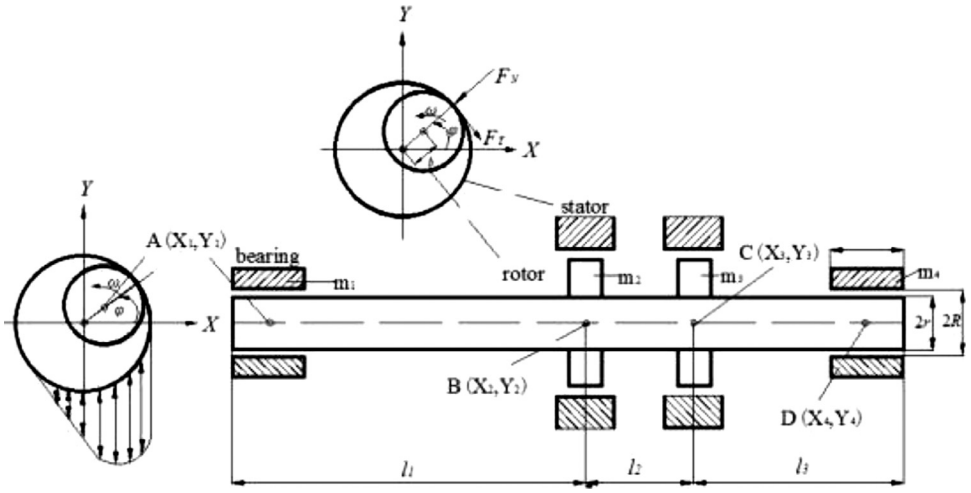

Fig. 1. Rotor-bearing system with two asymmetric discs.

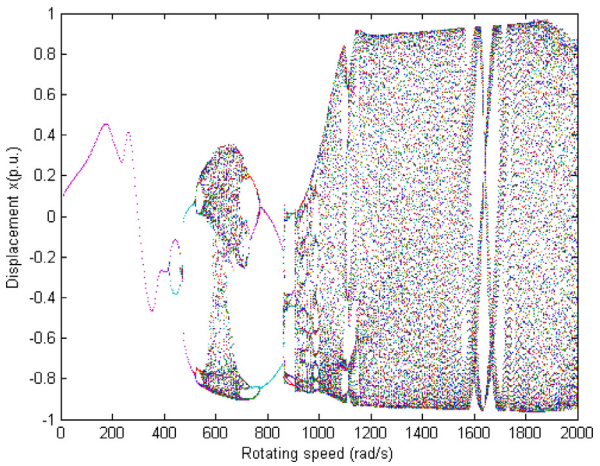

Fig. 2. Bifurcation diagram at $b_3 = 0.1$ mm and $K_c = 7 \times 10^6 N \cdot m^{-1}$.

presented in this paper. The influence of unbalance and rub-impact forces on oil-film instability is researched. Model of unbalanced rotor-bearing system with two asymmetric discs is established. The orbits of shaft, Poincare maps, largest Lyapunov exponent, waterfall curves of analog signals and bifurcation diagrams, etc. are constructed to analyze the dynamic characteristic of rotor-bearing system. Numeral results reveal a nonlinear dynamic process including periodic, quasi-periodic, multi-periodic and almost-periodic. Furthermore, the results from the numeral experiment show that the oil-film fault instability can be restrained or even removed if unbalanced force or rub-impact force is changed in this rotor-bearing system.

2. Mathematical model

The model of rotor-bearing system consists of two discs at point *B* and *C* and a massless shaft mounted by two oil-film journal bearings at each end (point *A* and *D*), as shown in Fig. 1. The two discs have a lumped mass m_2 and m_3, while the two bearing take lumped mass m_1 and m_4. The influence of torsional vibration, shear deformation and gyroscopic couple are all neglected in order to highlight the effect of oil-film force.

2.1. Model of oil-film forces

In this study, the Reynolds-type equation and the short bearing assumption is used. The Reynolds equation can be modified and performed as [20]

$$\left(\frac{R}{L}\right)^2 \frac{\partial}{\partial Z}\left(h^3 \frac{\partial p}{\partial Z}\right) = x\sin\theta - y\cos\theta - 2(x'\cos\theta + y'\sin\theta) \tag{1}$$

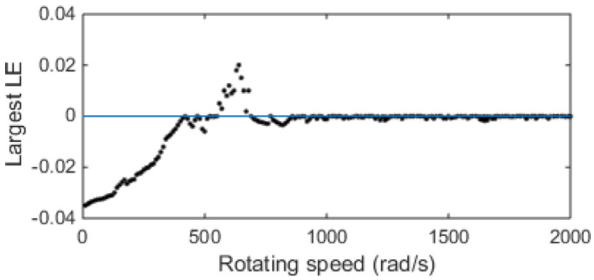

Fig. 3. Largest Lyapunov exponent at $b_3 = 0.1$ mm and $K_c = 7 \times 10^6 N \cdot m^{-1}$.

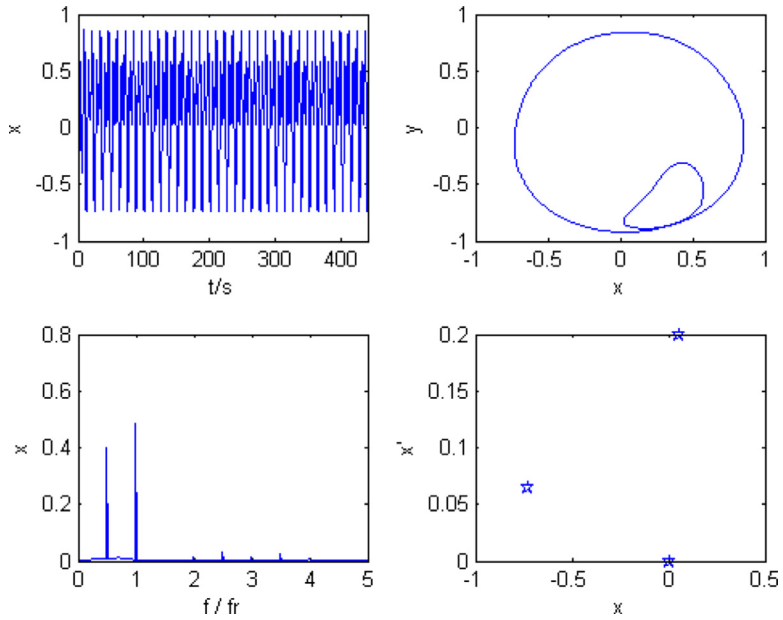

Fig. 4. Time series, shaft orbit, frequency spectra and Poincare map at $\omega = 500$ rad/s.

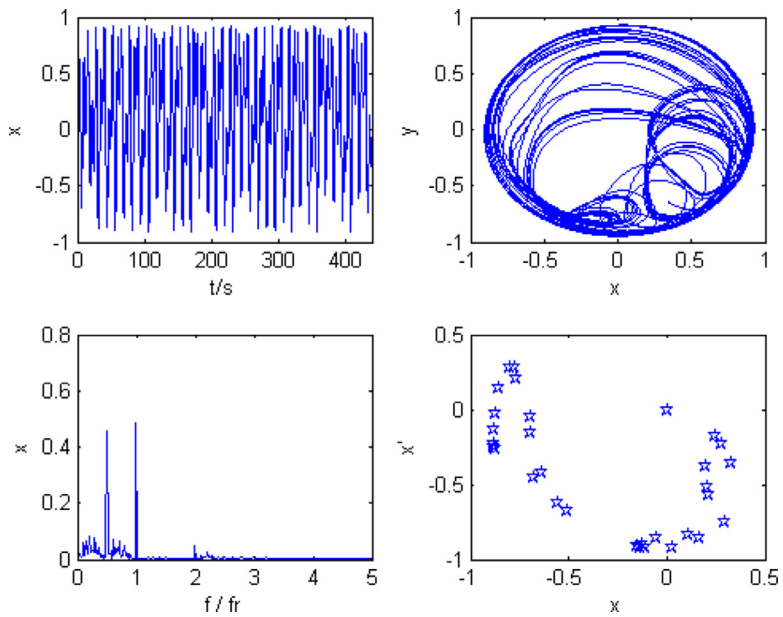

Fig. 5. Time series, shaft orbit, frequency spectra and Poincare map at $\omega = 650$ rad/s.

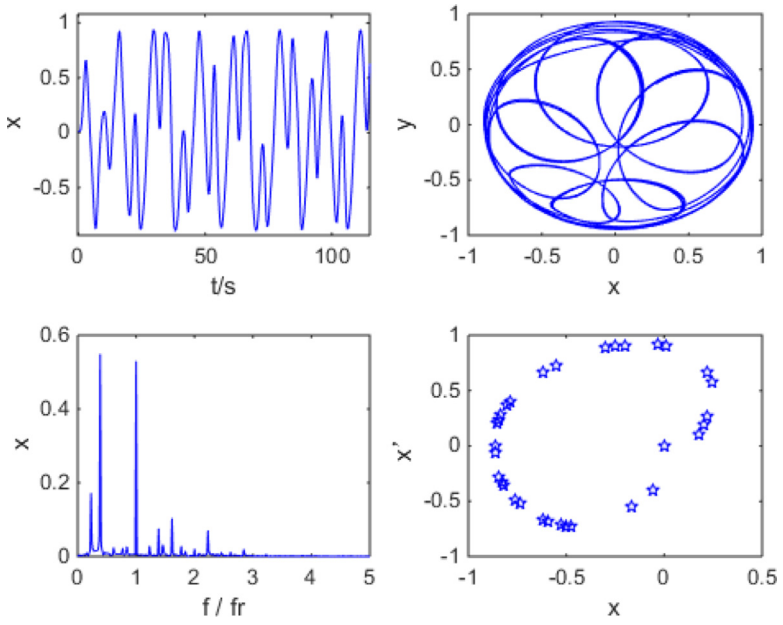

Fig. 6. Time series, shaft orbit, frequency spectra and Poincare map at $\omega = 1000$ rad/s.

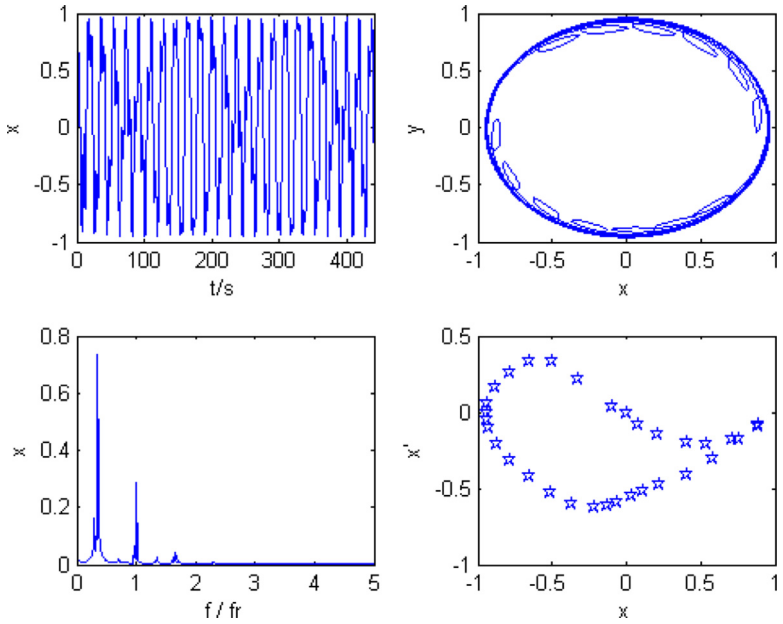

Fig. 7. Time series, shaft orbit, frequency spectra and Poincare map at $\omega = 1400$ rad/s.

Integrating the Reynolds Eq. (1), the distribution of oil film pressure is given as

$$p = \frac{1}{2}\left(\frac{L}{D}\right)^2 \frac{(x-2y')\sin\theta - (y+2x')\cos\theta}{(1-x\cos\theta - y\sin\theta)^3} \tag{2}$$

The non-dimension oil film force components $\overline{fx}$ and $\overline{fy}$ can be written as:

$$\begin{cases} f_X = \sigma \bar{f}_X; \\ f_Y = \sigma \bar{f}_Y \end{cases}$$

$$\sigma = \mu\omega RL\left(\frac{R}{c}\right)^2\left(\frac{L}{2R}\right)^2$$

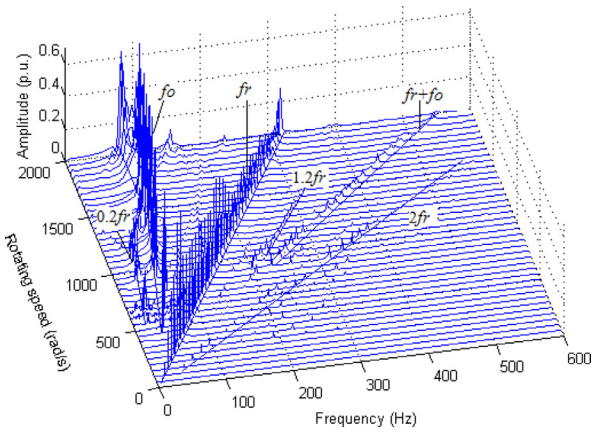

Fig. 8. Cascade spectrum of rotor-bearing system at $b_3 = 0.1$ mm and $K_c = 7 \times 10^6 N \cdot m^{-1}$.

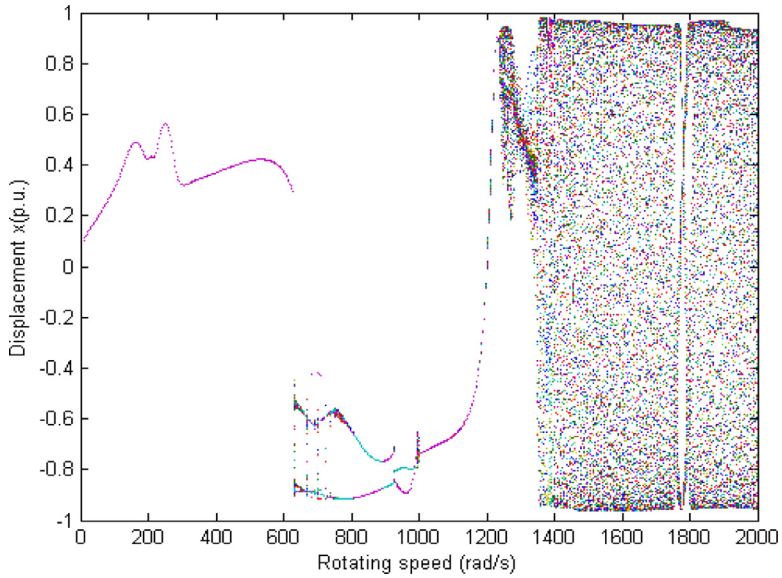

Fig. 9. Bifurcation diagram at $b_3 = 0.2$ mm.

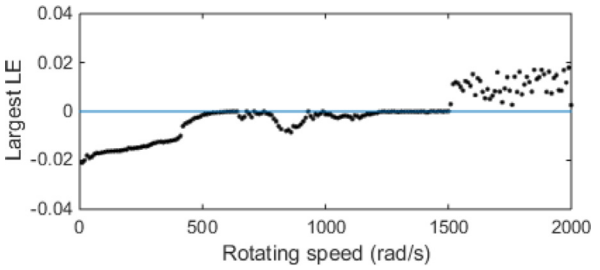

Fig. 10. Largest Lyapunov exponent at $b_3 = 0.2$ mm.

$$\begin{bmatrix} \bar{f}_x \\ \bar{f}_y \end{bmatrix} = -\frac{[(x-2\dot{y})^2 + (x+2\dot{x})^2]^{1/2}}{1x^2 - y^2} \times \begin{bmatrix} 3xV(x,y,\alpha) - \sin\alpha G(x,y,\alpha) - 2\cos\alpha S(x,y,\alpha) \\ 3xV(x,y,\alpha) + \cos\alpha G(x,y,\alpha) - 2\sin\alpha S(x,y,\alpha) \end{bmatrix} \tag{3}$$

Where R is the radius of bearing. c is the bearing radial clearance, μ is the lubricating oil viscosity described, and L is the length of bearing.

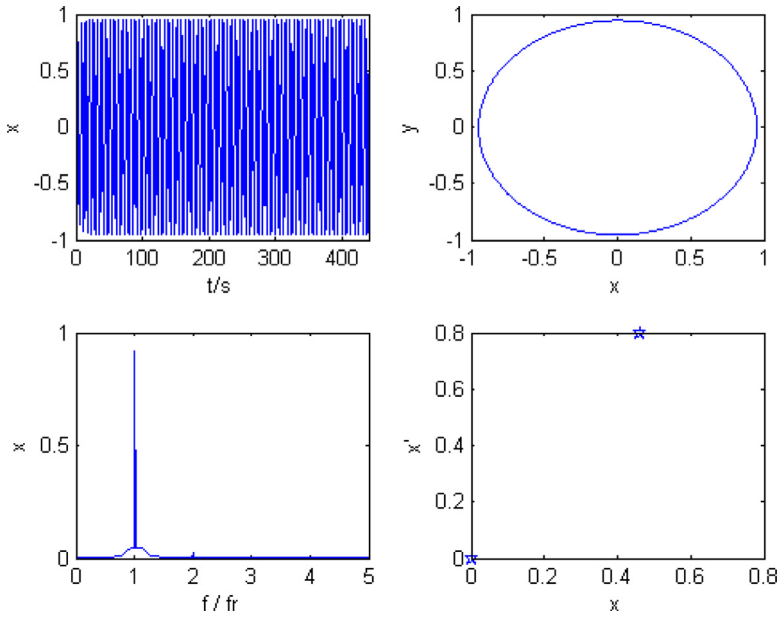

Fig. 11. Time series, shaft orbit, frequency spectra and Poincare map at $\omega = 500$ rad/s.

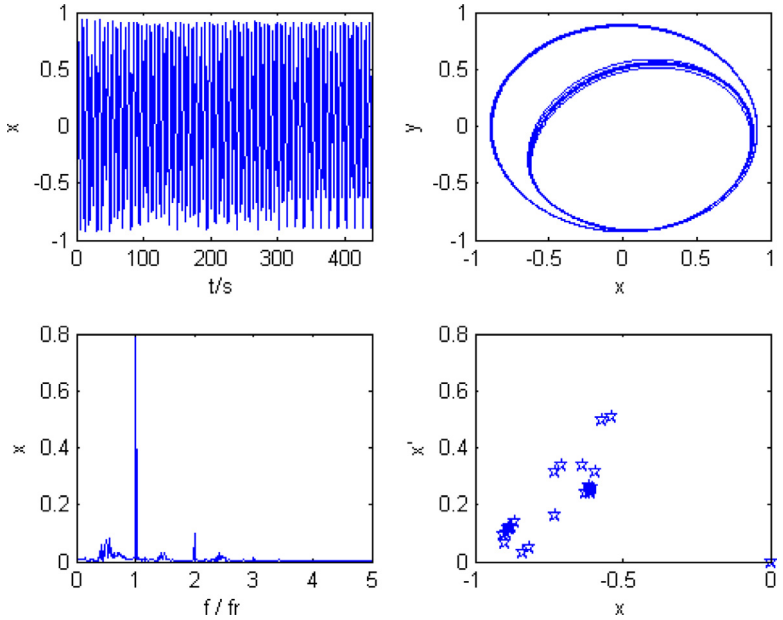

Fig. 12. Time series, shaft orbit, frequency spectra and Poincare map at $\omega = 700$ rad/s.

The non-dimensional parameters are introduced as below

$$\alpha = \arctan\frac{y+2\dot{x}}{x-2\dot{y}} - \frac{\pi}{2}\sin\left(\frac{y+2\dot{x}}{x-2\dot{y}}\right) - \frac{\pi}{2}\sin(y+2\dot{x})$$

$$V(x,y,\alpha) = \frac{2+(y\cos\alpha - x\sin\alpha)G(x,y,\alpha)}{1-x^2-y^2}$$

$$G(x,y,\alpha) = \frac{2}{(1-x^2-y^2)^{1/2}}\left[\frac{\pi}{2} + \arctan\frac{y\cos\alpha - x\sin\alpha}{1-x^2-y^2}\right]$$

$$S(x,y,\alpha) = \frac{x\cos\alpha + y\sin\alpha}{1-(x\cos\alpha + y\sin\alpha)^2} \tag{4}$$

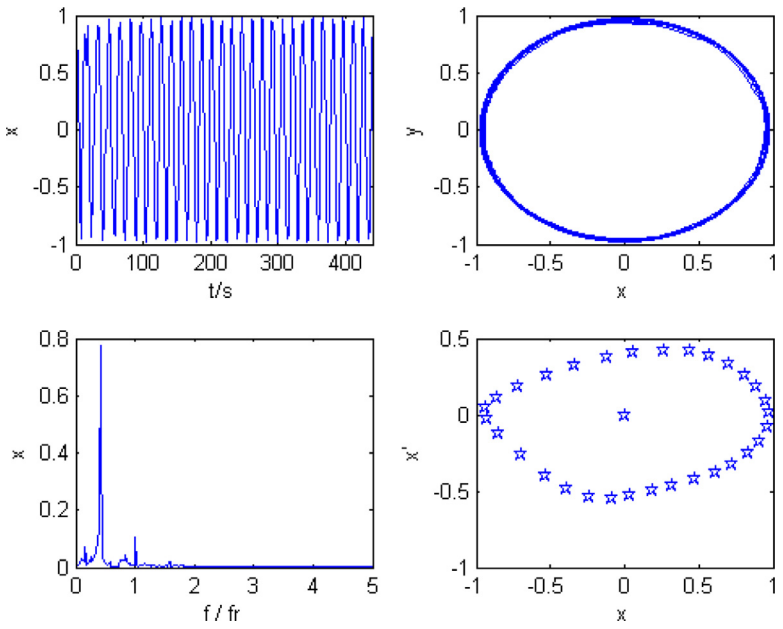

Fig. 13. Time series, shaft orbit, frequency spectra and Poincare map at $\omega = 1400$ rad/s.

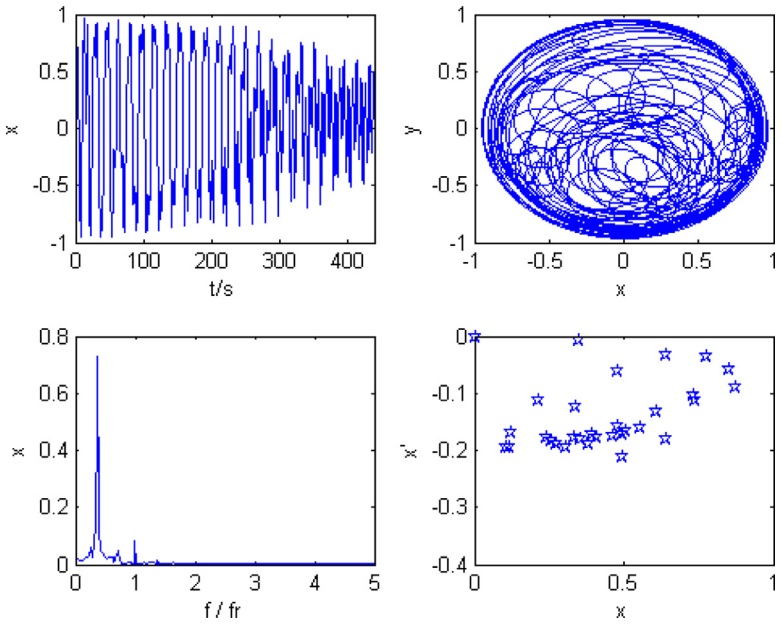

Fig. 14. Time series, shaft orbit, frequency spectra and Poincare map at $\omega = 1600$ rad/s.

2.2. Rub-impact forces

Rub-impact can bring about two forms forces integrated to be rub-impact force. One force called striking force F_N which is made by the contact of the rotor against stator. Another force is known as frictional force F_T. The rub-impact model of this rotor-bearing system is shown in Fig. 1. It's assumed that the rub-impact occurs with a Hertz contact and a Coulomb friction.

The striking force F_N is represented following linear elastic deformation theory. The frictional force F_T is brought up by coulomb law.

$$F_N = \begin{cases} 0, & (r < \delta) \\ (r-\delta)K_c, & (r \geq \delta) \end{cases}$$
$$F_T = fF_N \tag{5}$$

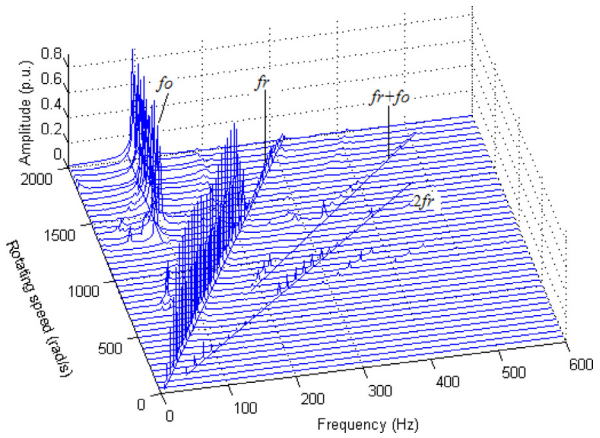

Fig. 15. Cascade spectrum of rotor-bearing system at $b_3 = 0.2$ mm.

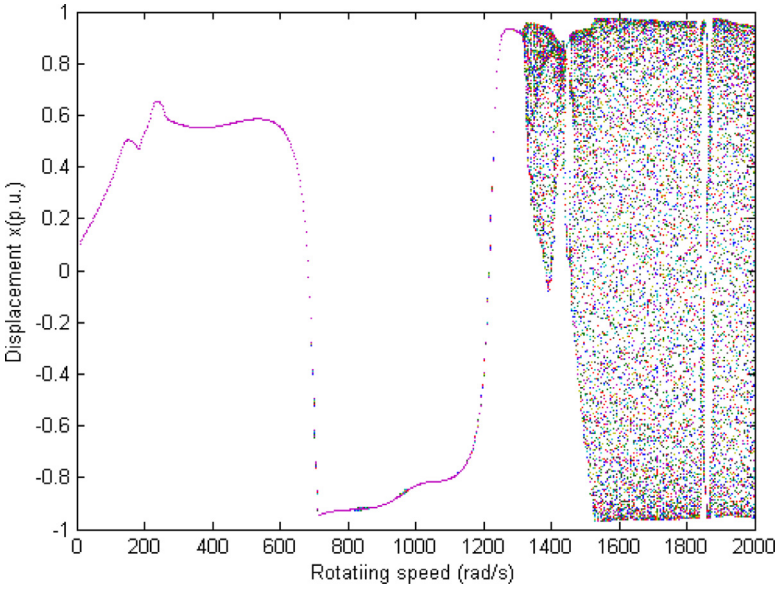

Fig. 16. Bifurcation diagram at $b_3 = 0.3$ mm.

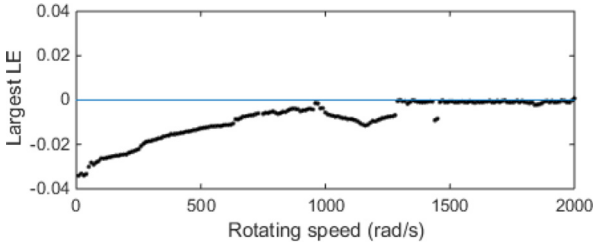

Fig. 17. Largest Lyapunov exponent at $b_3 = 0.3$ mm.

Where δ is the clearance between rotor and stator, r is the displacement of shaft center in radial direction and $r = \sqrt{x^2 + y^2}$.

The equations of rub-impact forces in x and y direction are formulated as follows:

$$\begin{pmatrix} F_x \\ F_y \end{pmatrix} = -\frac{r-\delta}{r} K_c \begin{pmatrix} 1 & -f \\ f & 1 \end{pmatrix} \begin{pmatrix} x \\ y \end{pmatrix} \quad (r > \delta) F_x = F_y = 0 \quad (r < \delta) \tag{6}$$

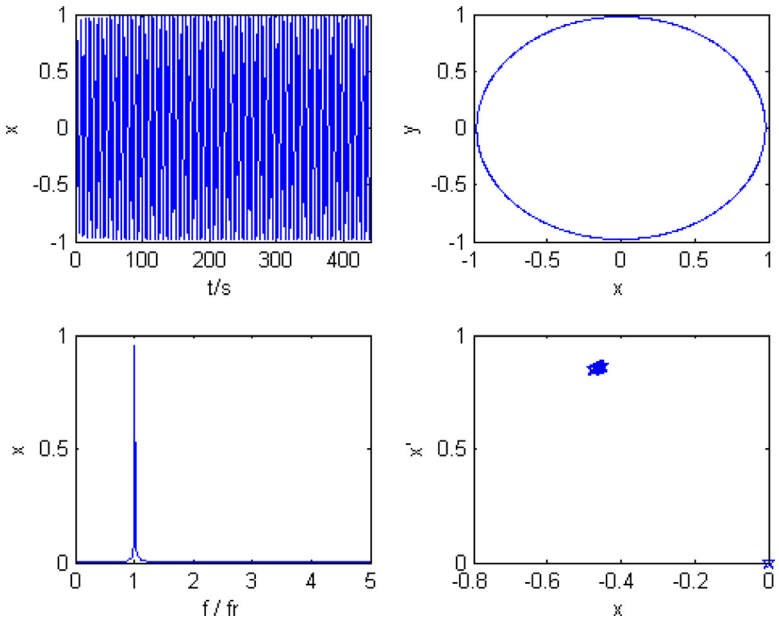

Fig. 18. Time series, shaft orbit, frequency spectra and Poincare map at $\omega = 700$ rad/s.

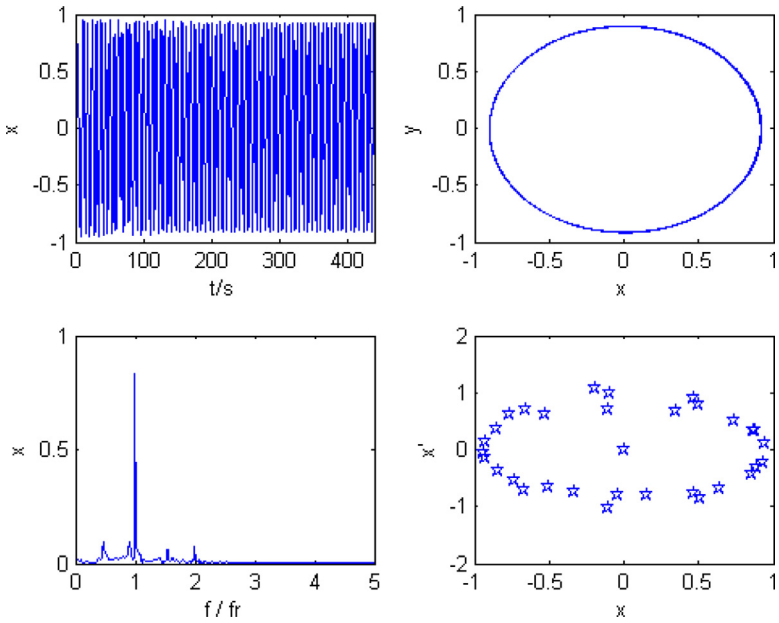

Fig. 19. Time series, shaft orbit, frequency spectra and Poincare map at $\omega = 1312$ rad/s.

2.3. Model of rotor-bearing system

The model of rotor-bearing system is shown in Fig. 1. The mathematical model based on rotor dynamics theory are established in Eq. (7)

$$\begin{aligned} &M\ddot{Z} + C\dot{Z} + KZ = F_o + F_e + F_g + F_p \\ &F_o, F_e, F_g, F_p \in C^4 \end{aligned} \tag{7}$$

Where M,C,K are mass, damping and stiffness matrix, Matrix $Z = [Z_1, Z_2, Z_3, Z_4]^T \in C^4(Z_i = x_i + jy_i)$ is the displacement matrix corresponding to each mass. The damping coefficient of the ith mass is c_i.

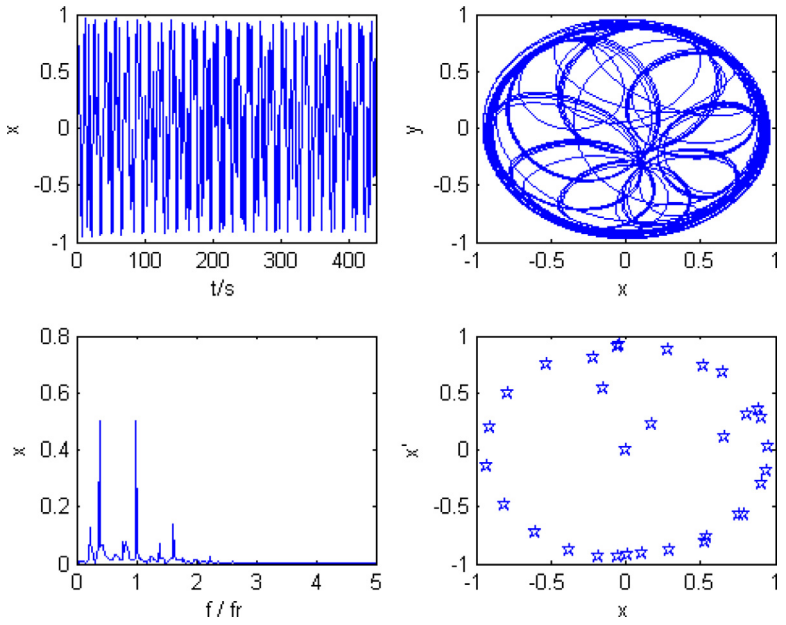

Fig. 20. Time series, shaft orbit, frequency spectra and Poincare map at $\omega = 1400$ rad/s.

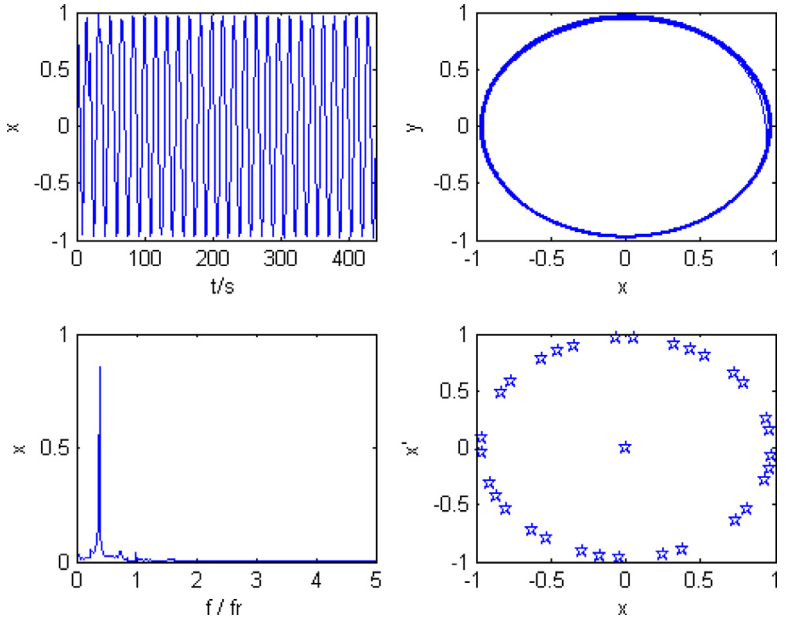

Fig. 21. Time series, shaft orbit, frequency spectra and Poincare map at $\omega = 1600$ rad/s.

$M = diaf[m_i](i = 1, 2, 3, 4)$ $C = diag[c_i](i = 1, 2, 3, 4)$ The stiffness matrix is:

$$\mathrm{K} = \begin{bmatrix} k_1 & -k_1 & & \\ -k_1 & k_1 + k_2 & -k_2 & \\ & -k_2 & k_2 + k_3 & -k_3 \\ & & -k_3 & k_3 \end{bmatrix} \tag{8}$$

The stiffness of each axis according to structural relationships of plane beam is as follows: the stiffness of support axis in both ends is $k_i = 3EI_i/{l_i}^3, i = 1, 3$, and the stiffness of middle axis is $k_i = 12EI_i/{l_i}^3, i = 2$. I_i is the section inertia of that axis and the symbol l_i is the length of each axis.

$$I_i = \frac{\pi d_i^4}{64} (i = 1, 2, 3) \tag{9}$$

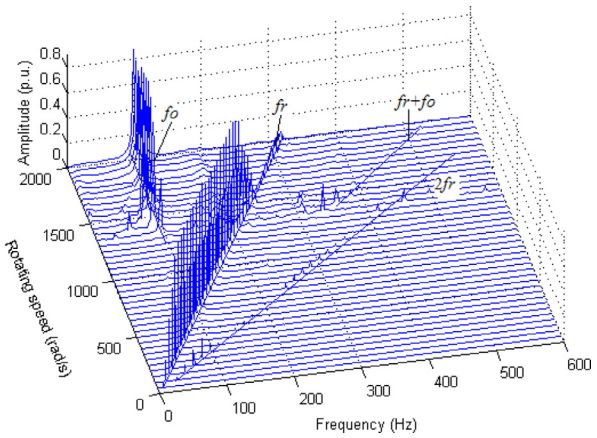

Fig. 22. Cascade spectrum of rotor-bearing system at $b_3 = 0.3$ mm.

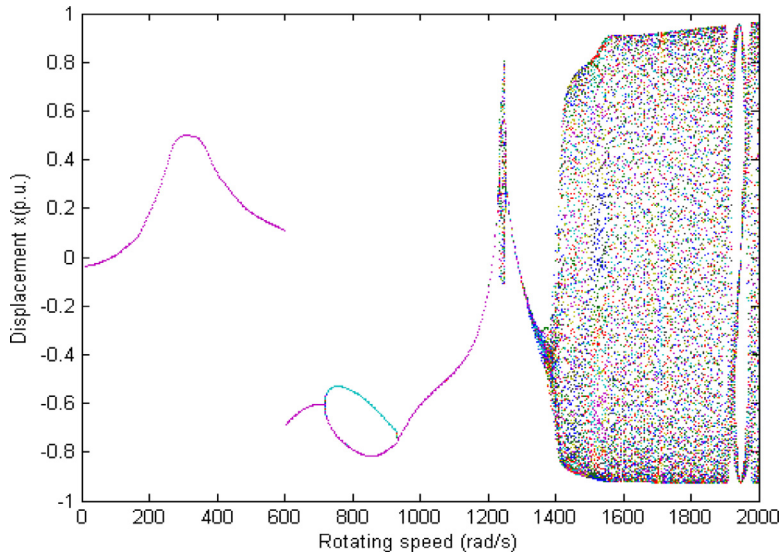

Fig. 23. Bifurcation diagram at $K_c = 9 \times 10^6 N \cdot m^{-1}$.

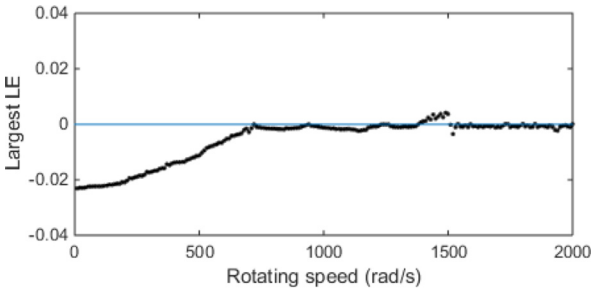

Fig. 24. Largest Lyapunov exponent at $K_c = 9 \times 10^6 N \cdot m^{-1}$.

Where d_i is the diameter of section in each axis. Notations F_o, F_e, F_g, $F_p \in C^4$ are the plural oil-film force, plural unbalance, plural gravity and plural rub-impact force matrix:

$$
\begin{aligned}
F_o &= [F_{o1}\,0\;0\;F_{O4}]^T \\
F_p &= [0\;F_{p2}\;F_{p3}\;0]^T \\
F_e &= [0\;F_{ex}\;F_{ey}\;0]^T \\
F_g &= -jg[m_1\;m_2\;m_3\;m_4]^T
\end{aligned} \tag{10}
$$

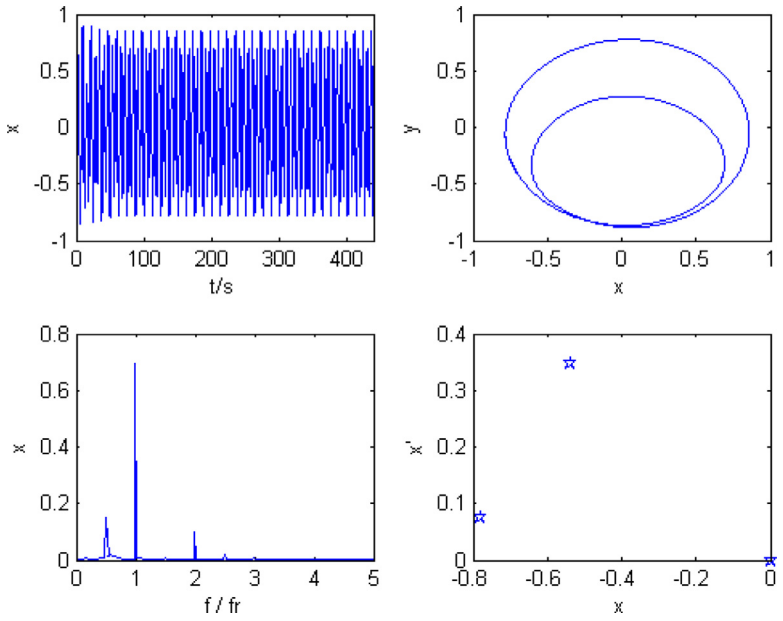

Fig. 25. Time series, shaft orbit, frequency spectra and Poincare map at $\omega = 800$ rad/s.

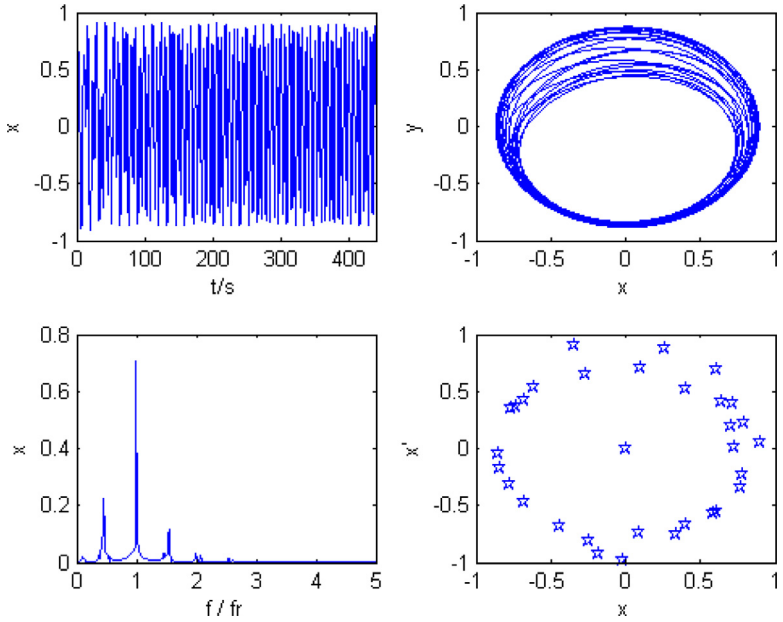

Fig. 26. Time series, shaft orbit, frequency spectra and Poincare map at $\omega = 1240$ rad/s.

The unbalanced eccentric force is:

$$\begin{bmatrix} F_{exi} \\ F_{eyi} \end{bmatrix} = \begin{bmatrix} m_i e_i \omega_r{}^2 \cos(\omega_r t + \phi_i) \\ m_i e_i \omega_r{}^2 \sin(\omega_r t + \phi_i) \end{bmatrix}, \quad i = 2, 3 \tag{11}$$

Where b_2 and b_3 are the mass eccentricity of discs.

3. Nonlinear dynamic analysis

The numerical solution of Eq. (7) is carried out by using fourth-order Runge–Kutta method. In the investigation, the time step for direct numerical integration is specified as $\pi/200$. The system parameters are used in Table 1. The bifurcation diagrams, system time series, shaft orbit, Poincaré maps, frequency spectra and cascade spectrum are obtained by numerical integration.

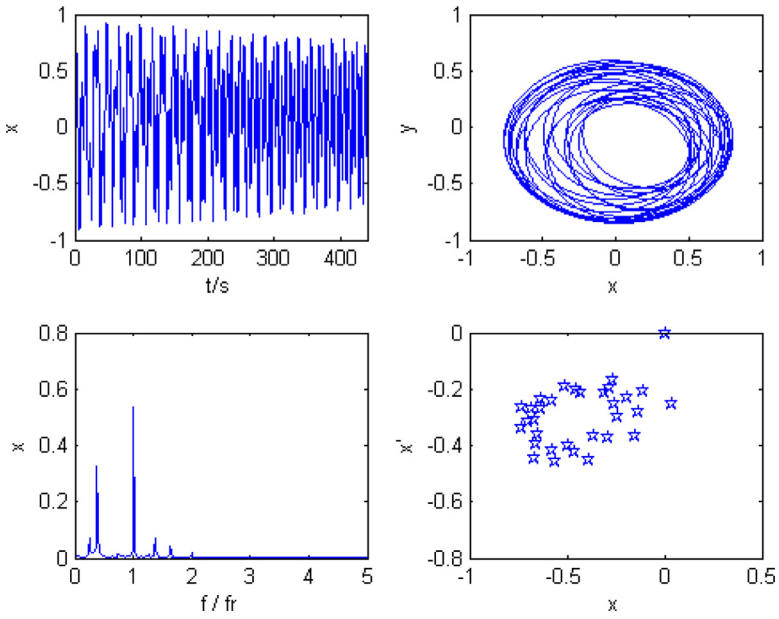

Fig. 27. Time series, shaft orbit, frequency spectra and Poincare map at $\omega = 1400$ rad/s.

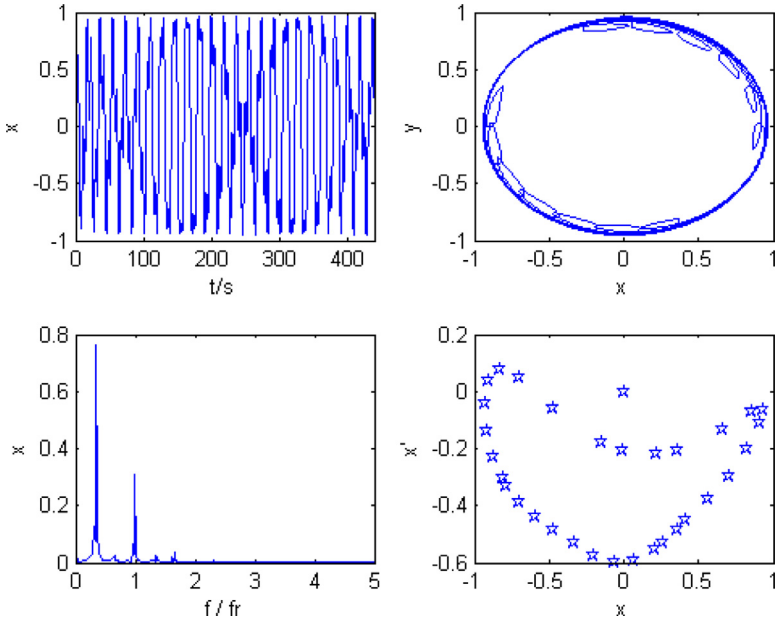

Fig. 28. Time series, shaft orbit, frequency spectra and Poincare map at $\omega = 1800$ rad/s.

Poincare maps can provide a powerful method for diagnostic purposes since they can provide information which is obtained unsuccessfully from either the shaft orbit or the frequency spectra of the rotor response.

3.1. Response of rotor-bearing system with varying rotating speed

The bifurcation diagram and largest Laypunov exponent of rotor-bearing system are separately shown in Figs. 2 and 3 with ω as control parameter. All the parameters are taken from Table 1. The rotor-bearing system is found to display a rich diversity of responses with very intricate dynamics. The dynamic motion of this system is synchronous with period-one (P1) before $\omega = 418$ rad/s. The period-two (P2) is observed at $\omega = [418 \sim 520]$ rad/s. It can be seen in Fig. 4 where the shaft orbit has two oval, the frequency spectra has two discrete frequency components and the Poincare maps has two offset points. Therefore there are oil-whirl and rub-impact at this rotating speed region already (see Fig. 8). It takes the general form {P4→P8…chaos→P8→P4→P2}

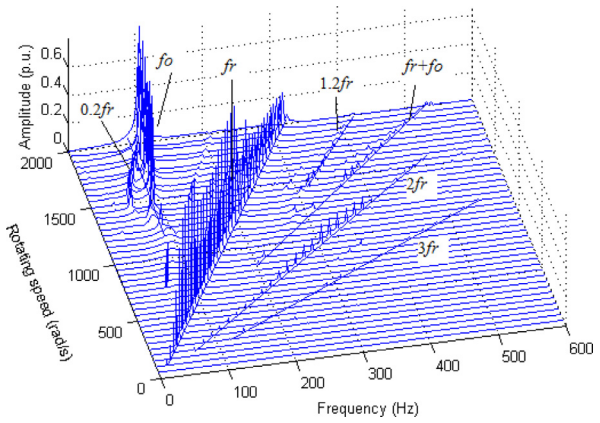

Fig. 29. Cascade spectrum of rotor-bearing system at $K_c = 9 \times 10^6 N \cdot m^{-1}$.

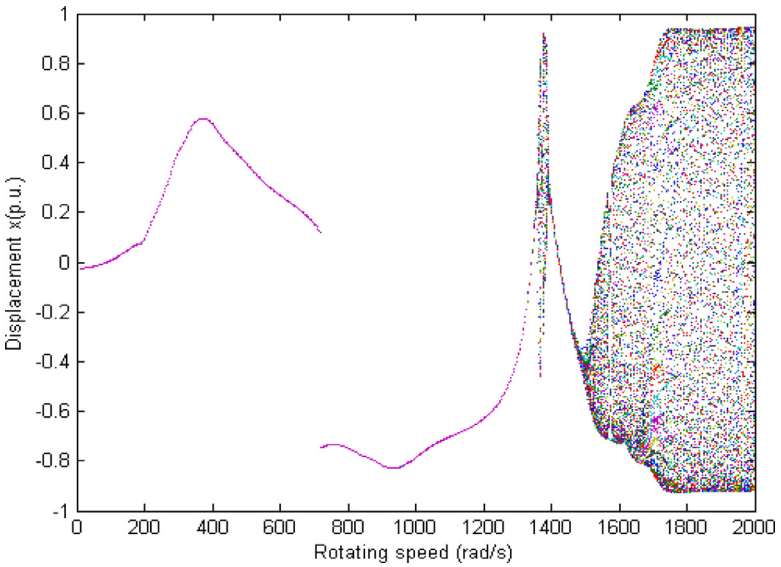

Fig. 30. Bifurcation diagram at $K_c = 1.1 \times 10^7 N \cdot m^{-1}$.

as the rotating speed is varied between the values [520→865] rad/s. The classic oil-whirl shaft orbit turns up in Fig. 5 at $\omega = 650$ rad/s. The half-frequency amplitude almost equals the amplitude of fundamental frequency. And there are continuous frequency bands on the frequency spectra. Two strange attractors appear in Poincare map. Hence the system is caught in chaos which also can be concluded by the largest Lyapunov exponent, which is greater than zero if chaos occurred (Shown in Fig. 3).

The system experiences multiple periodic and quasi-periodic motions at $\omega \geq 865$ rad/s. Oil-whip occurs at $\omega = 1000$ rad/s (See Fig. 6). The oil-whirl frequency is lesser than half of rotating speed frequency which can be inferred as oil-whip frequency. Moreover, there is much multi-frequency on the spectra caused by worse rub-impact. The system motion is entering quasi-periodic motion seen in the Poincaré map. And the quasi-periodic motion is undergoing when $\omega = 1400$ rad/s deduced by the Poincaré map in Fig. 7. There are distinct "beat" signals in time series. The amplitude of oil-whip frequency is considerably larger than that of fundamental frequency. Corresponding with the bifurcation in Fig. 2, Fig. 8 reveals the whole vibration journey of system. Fig. 8 named cascade spectrum is one of three-dimension frequency spectra in which the third dimension is rotating speed. The cascade spectrum can help to observe the vibration frequency characteristics when the speed of the system has changed in different operation state. The oil-whirl frequency appears at $\omega = 450$ rad/s, increases as half of fundamental frequency, and turns into oil-whip frequency ($f0$) at $\omega = 1000$ rad/s. Meanwhile, the rub-impact gets stronger.

3.2. Influence of eccentricity magnitude

Fig. 9 represents the bifurcation diagram at a higher eccentricity ($b_3 = 0.2$ mm) for comparison with Fig. 2 ($b_3 = 0.1$ mm). In this case, the responses of this system exhibit simpler dynamic phenomena. Shown both in bifurcation and largest Lyapunov exponent (see Fig. 10), the system takes a series of motions {P1→Pn→P2→P3→P1→quasiperiod→chaos}. Larger imbalance

Table 1
The simulated model parameters of rotor-bearing system.

Parameters	values
m_1, m_2, m_3, m_4 (Kg)	0.055, 0.8, 0.8, 0.1176
l_1, l_2, l_3 (m)	0.2475, 0.0375, 0.06
c, D, L, d, b (mm)	0.275, 25, 25, 10, 0.1
c_1, c_2, c_3, c_4 $(N \cdot s \cdot m^{-1})$	1000, 2000, 2000, 1000
K_c $(N \cdot m^{-1})$	7×10^6
η(Pa · s)	0.04

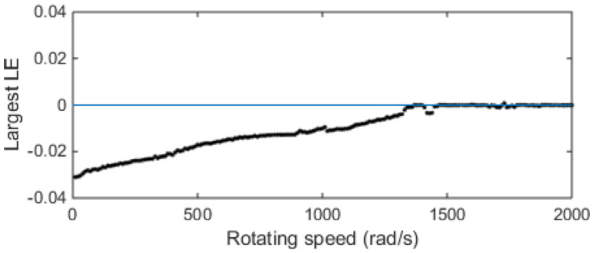

Fig. 31. Largest Lyapunov exponent at $K_c = 1.1 \times 10^7 N \cdot m^{-1}$.

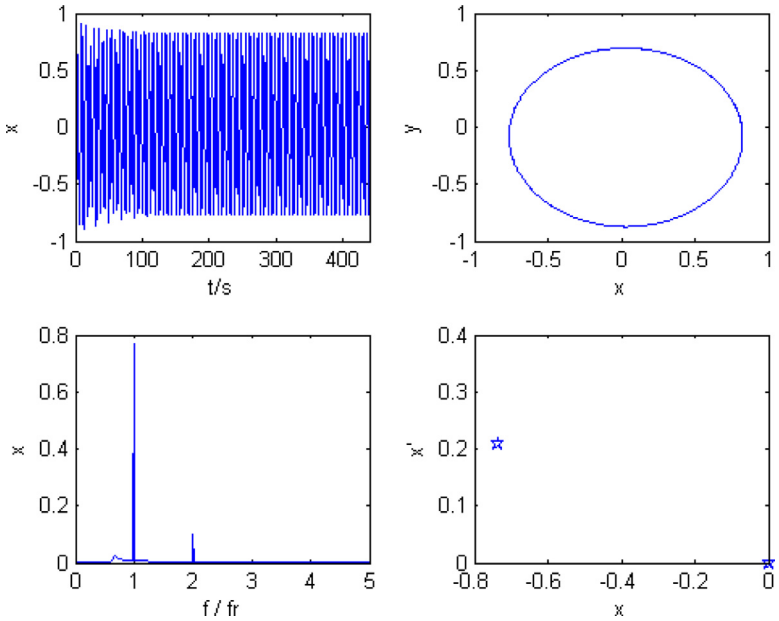

Fig. 32. Time series, shaft orbit, frequency spectra and Poincare map at $\omega = 800$ rad/s.

force may simplify the system motion at a same rotating speed. The dynamic response undergoes synchronous vibration with period-one until $\omega = 634$ rad/s (see Fig. 11). When the $\omega = [634 \sim 1000]$ rad/s, oil-whirl arises with a small value and the motion is multiple periodic (see Fig. 12). The system experiences period-one motion at $\omega = [1000 \sim 1240]$ with only rub-impact. After the oil-whip occurs, the system vibrations go through quasi-periodic and chaotic motion (see Figs. 10, 13 and 14). The frequency components of oil-whip are uninfluenced but the frequency components of oil-whirl are restrained when the imbalance force increases. In this circumstance, the frequency components of rub-impact exist in all way (see Fig. 15).

The eccentricity further adds to 0.3 mm. It reveals a more brief vibration curve in the bifurcation diagram and largest Lyapunov exponent (see Figs. 16 and 17). Neither oil-whirl nor oil-whip comes up until $\omega = 1312$ rad/s. And the system take motion with P1 (see Fig. 18). It shows a typical Hopf bifurcation at $\omega = 1312$ rad/s (see Fig. 19) and oil-whip takes place later and the system motion becomes quasi-periodic (see Figs. 20 and 21). It is shown distinctly in Fig. 22 that there are only fundamental frequency and rub-impact frequency when $\omega \leq 1312$ rad/s. After the speed, the oil-whip appears and occupies most energy of the system. We can also obtain the same conclusions that the oil-whirl is restrained but the oil-whip is uninfluenced, when the imbalance force increases (see Fig. 22).

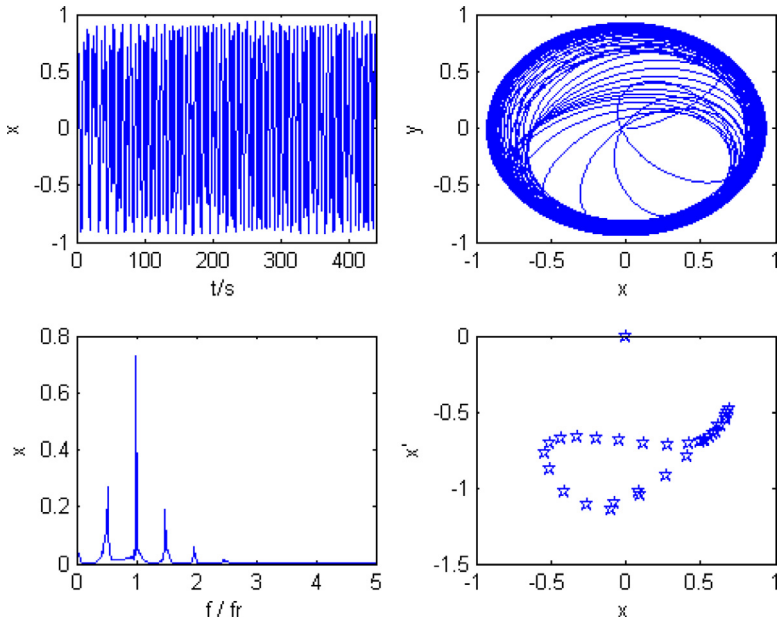

Fig. 33. Time series, shaft orbit, frequency spectra and Poincare map at $\omega = 1360$ rad/s.

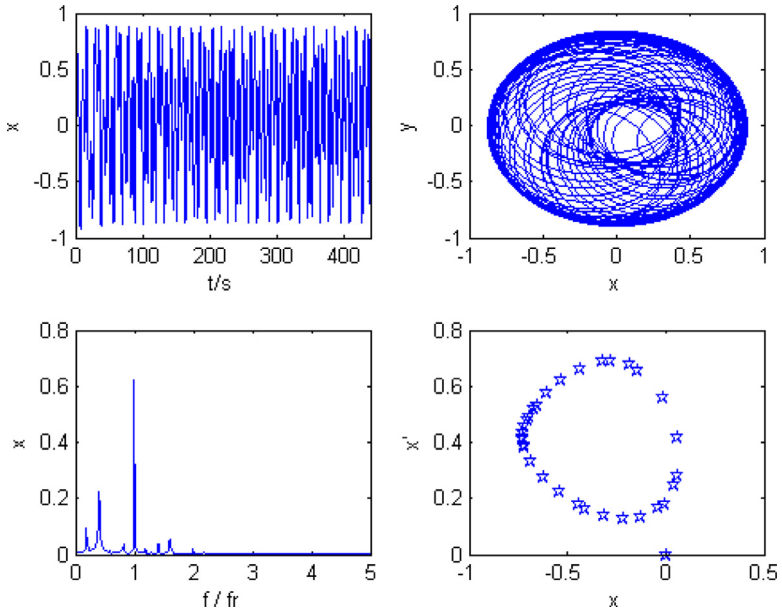

Fig. 34. Time series, shaft orbit, frequency spectra and Poincare map at $\omega = 1550$ rad/s.

3.3. Influence of stator stiffness size

In this study, the stator stiffness is introduced, which is in direct proportion to the rub-impact force size. It has been discovered that it plays a significant role in vibration analysis of rotor with rub-impact. Bifurcation diagram and largest Lyapunov exponent with varying rotating speed of this system for stator stiffness parameter $K_c = 9 \times 10^6 N \cdot m^{-1}$ is shown in Figs. 23 and 24. The nonlinear motion components have become less than $K_c = 7 \times 10^6 N \cdot m^{-1}$ in Fig. 2. In the entire rotating speed arising region [0∼2000] rad/s, the system experiences a vibration journey as {P1→P2→P1→ quasi-period→P1→ chaos→ quasi-period}. Period-two exists at $\omega = [721 \sim 941]$ rad/s while slight oil-whirl being in system. And rub-impact frequency also is present on the frequency spectra (see Fig. 25). The rotor system accesses quasi-periodic motion by Neimark–Sacker bifurcation when $.\omega = 1240.$rad/s (see Fig. 26). After that the system undergoes a small rotating speed period until it goes in to chaos at $\omega = 1400$ rad/s (see Figs. 24 and 27). And the quasi-periodic motion is taken by

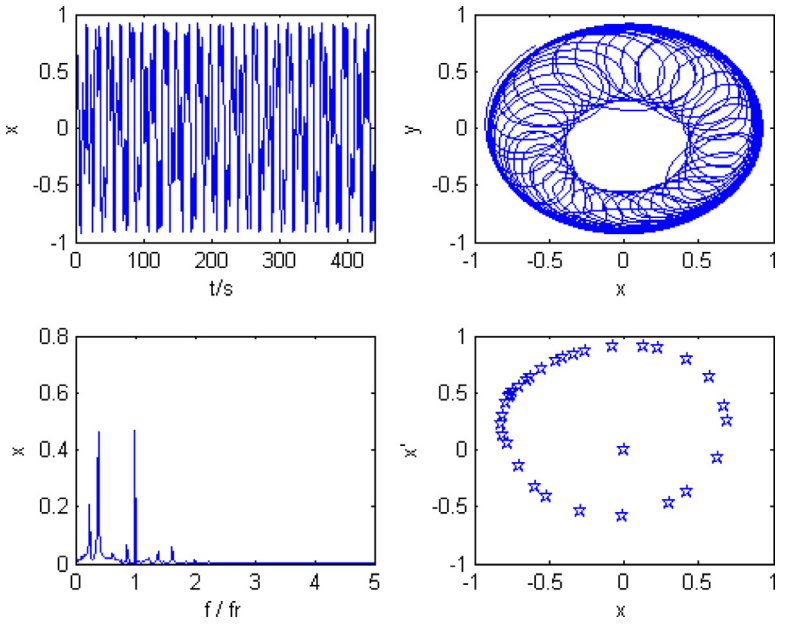

Fig. 35. Time series, shaft orbit, frequency spectra and Poincare map at $\omega = 1700$ rad/s.

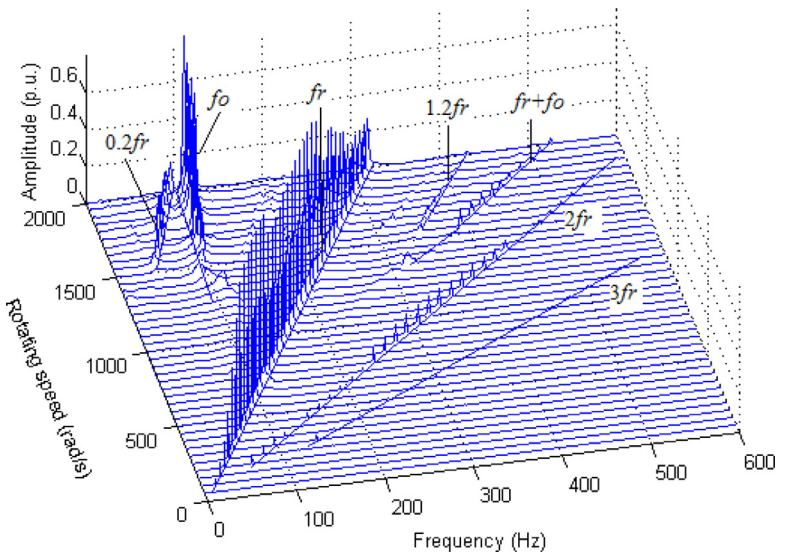

Fig. 36. Cascade spectrum of rotor-bearing system at $K_c = 9 \times 10^6 N \cdot m^{-1}$.

this system eventually (see Fig. 28). The cascade spectrum of system demonstrates that oil-whirl frequency range decreases at larger stator stiffness but the oil-whip frequency does not change (see Fig. 29. Meanwhile the rub-impact frequency is enhanced.

To further discover the dynamical influence of the stator stiffness to coupled system, the stator stiffness is added to $K_c = 1.1 \times 10^7 N \cdot m^{-1}$, and the bifurcation and largest Lyapunov exponent of system is displayed in Figs. 30) and 31. The nonlinear behaviors get simpler than that the stator stiffness takes two less values before. Analyzing the largest Lyapunov exponent and all the characteristic pictures (see Figs. 32–35) synthetically, it is found that the system motion goes through a process {P1→quasi-period→P1→quasi-period}. The oil-whirl motion does not occur. The oil-whip frequency comes out about at $\omega = 1350$ rad/s and keeps a uniform value when $\omega \geq 1350$ rad/s (see Fig. 36). Rub-impact frequencies get higher amplitude with this bigger stator stiffness.

4. Conclusion

A nonlinear model has been formulated in order to explore the coupled behaviors of the asymmetric double-disc rotor-bearing system with interaction between rub-impact and oil-film force. The modeling strategy of our approach employed the short bearing theory to describe the oil film force and assumed the rub-impact as a Hert contact a Coulomb friction. Considering nonlinear oil-film force and rub-impact force, the mathematical model of the asymmetric double-disc rotor-bearing system is described in dynamics theory. The numerical results indicated that the studied system exhibited rich nonlinear phenomena, such as the period-doubling bifurcation, the multi-period and the quasi-periodic motions. The comparison of the dynamic behavior with different parameters revealed that eccentricity and stator stiffness affected the vibration and instability of the system with varied rotating speed. In conclusion, when magnify eccentricity increases, the motion of system becomes simple and the oil-whirl is restrained or even removed, but the oil-whip is uninfluenced. When the value of stator stiffness increases, the motion of system also becomes simple and the oil-whirl gets weak or even removed. In any way, the characters of rub-impact exist at all times. The results indicate that the fault forces can be interacted and the system with different faults may have self-healed phenomena. Now we are employing the experiment of the test rig to validate the numerical results.

Acknowledgment

This work is supported by the National Natural Science Foundation of China (No. 51475164 and 11072078) and Natural Science Foundation of Hebei Province (E2013502226).

References

[1] F.F. Ehrich, Some observations of chaotic vibration phenomena in high-speed rotordynamics, ASME J. Vib. Acoustics 113 (1991) 50–57.
[2] H. Diken, Non-linear vibration analysis and subharmonic whirl frequencies of the Jeffcott rotor model, J. Sound Vib. 243 (2001) 117–125.
[3] C.C. Wang, C.Y. Lo, C.K. Chen, Nonlinear dynamic analysis of a flexible rotor supported by externally pressurized porous gas journal bearings, ASME J. Tribology 124 (2002) 553–561.
[4] H.F. de Castro, Whirl and whip instabilities in rotor-bearing system considering a nonlinear force model, J. Sound Vib. 317 (1-2) (2008) 273–293.
[5] J.P. Jing, On the oil-whipping of a rotor-bearing system by a continuum model, Appl. Math. Model. 29 (5) (2005) 461–475.
[6] X. Wenhui, Analysis of motion stability of the flexible rotor-bearing system with two unbalanced disks, J. Sound Vib 310 (1-2) (2008) 381–393.
[7] H. Taplak, Experimental analysis on fault detection for a direct coupled rotor-bearing system, Measurement 46 (1) (2013) 336–344.
[8] M. Cheng, Numerical and experimental study of a rotor–bearing–seal system, Mech. Machine Theory 42 (8) (2007) 1043–1057.
[9] C.-C. Fan, et al., Study of start-up vibration response for oil whirl, oil whip and dry whip, Mech. Syst. Signal Proc. 25 (8) (2011) 3102–3115.
[10] A. Muszynska, Rotor-to-stationary element rub-related vibration phenomena in rotating machinery literature survey, Shock Vib. Digest 21 (1989) 3–11.
[11] P Goldman, Muszynska, A. Chaotic behavior of rotor/stator systems with rubs, J. Eng. Gas Turbines Power 116 (1994) 692–701.
[12] F. Chu, Z. Zhang, Bifurcation and chaos in rub-impact jeffcott rotor system, J. Sound Vib. 210 (1) (1998) 1–18.
[13] Abu-Mahfouz Issam, Amit Banerjee, On the investigation of nonlinear dynamics of a rotor with rub-impact using numerical analysis and evolutionary algorithms, Procedia Comput. Sci. 20 (2013) 140–147.
[14] C.-W. Chang-Jian, C.-K. Chen, Chaos and bifurcation of a flexible rub-impact rotor supported by oil film bearings with nonlinear suspension, Mech. Machine Theory 42 (2007) 312–333.
[15] S. Lahriri, I. Ferreira Santos, Experimental quantification of contact forces with impact, friction and uncertainty analysis, Tribology Int. 66 (2013) 93–104.
[16] S. Lahriri, I.F. Santos, Theoretical modelling, analysis and validation of the shaft motion and dynamic forces during rotor–stator contact, J. Sound Vib. 332 (2013) 6359–6376.
[17] C.-W. Chang-Jian, C.-K. Chen, Couple stress fluid improve rub-impact rotor-bearing system– nonlinear dynamic analysis, Appl. Math. Model. 34 (2010) 1763–1778.
[18] Q. Lin, Z. Wei, W. Chen, Analysis on the lubrication performances of journal bearing system using computational fluid dynamics and fluid–structure interaction considering thermal influence and cavitation, Tribology Int. 64 (2013) 8–15.
[19] L. Wang, D.Q. Cao, W. Huang, Nonlinear coupled dynamics of flexible blade–rotor–bearing systems, Tribology Int. 43 (2010) 759–778.
[20] G. Adiletta, A.R. Guido, C. Rossi, Chaotic motions of a rigid rotor in short journal bearings, Nonlin. Dyn. 10 (6) (1996) 251–269.